Int J Adv Manuf Technol (2016) 86:2723–2733
DOI 10.1007/s00170-016-8347-4

ORIGINAL ARTICLE

Numerical and experimental investigation on the weld-induced deformation and residual stress in stiffened plates with brackets

Bai-Qiao Chen[1] · **C. Guedes Soares**[1]

Received: 8 October 2015 / Accepted: 11 January 2016 / Published online: 29 January 2016

Abstract The objective of this work is to access the importance of an accurate prediction of the weld-induced residual stresses and deformations based on numerical simulations and experiments. After the welding tests of stiffened plates with and without triangular brackets, the weld-induced deformation and residual stresses are numerically investigated by a nonlinear thermo-elasto-plastic approach. The present numerical results of the temperature distributions and vertical deformation show good agreement with the experimental measurements. The empirical formula proposed in the present work is proved to have the ability to provide accurate prediction of the residual stress distributed in the stiffened plate. It is concluded that the presence of the brackets has small influence on the residual stress distribution in the stiffened plate, whereas the maximum deformation of the studied stiffened plate with two transverse brackets reduces 74 % in the experimental measurements and 67 % in the numerical simulation.

Keywords Fillet welding · Experiment · Finite element analysis · Residual stress · Welding deformation

1 Introduction

Stiffened plates are key structural elements in marine and offshore structures, being widely used in a variety of lightweight structures due to their high strength-to-weight ratio and the relative simplicity of fabrication. During the fabrication of stiffened plates, a significant amount of fusion welding is required and the resulting out-of-plane deformation and residual stress induced by the welding process are a severe design penalty.

Extremely high temperature occurs during the welding process due to local heating. As the temperature of the weld increases, the yield strength, the modulus of elasticity and the thermal conductivity of the steel decrease, whereas the specific heat and the coefficient of thermal expansion increase [1]. The expansion and contraction of the weld metal and adjacent base metal during the heating and subsequent cooling cycle of the welding process result in distortions in the welded structures. Excessive distortion of welded components results in misalignment of parts and often requires costly remedial measures such as flame straightening and cold bending to reduce distortions to an acceptable level [2].

In recent years, there is a growing concern regarding the measurement, prediction and mitigation of weld-induced distortions. Results of many years of measurements of post-welding distortions of ship hull shell plating were published based on 1998 plates of general cargo ships, multi-purpose tugs, bulk carriers, chemical carriers, tankers, research vessels as well as passenger cargo ferries [3]. While this work used a traditional direct measurement, close-range photogrammetry has been used more recently to obtain an accurate measurement of the welding distortions in stiffened plates and box girders [4, 5], in which the three-dimensional (3D) displacement field of the plated structure is generated from sets of digital images.

Over the past years, numerical analysis such as finite element method (FEM) has been widely used to investigate the distribution of weld-induced distortions in structures. To model the moving heat source during the welding process, the double ellipsoidal mathematic model [6–8] and element birth and death feature [9] is commonly adopted. The main

✉ C. Guedes Soares
c.guedes.soares@centec.tecnico.ulisboa.pt

[1] Centre for Marine Technology and Ocean Engineering (CENTEC), Instituto Superior Técnico, Universidade de Lisboa, Lisbon, Portugal

Table 1 Configuration of stiffened plates (unit: mm)

	Associated plate	Stiffener	Bracket
Length	500	500	140
Width/height	350	150	140
Thickness	9	9	4

technique to solve the heat transfer problem was changing with the rapid growth in computer performance in the early 1970s when Ueda et al. [10] started to calculate the welding residual stress by FEM using 2D models. Michaleris and Debiccari [11] performed a thermo-elasto-plastic FEM to predict the welding distortion. The approach was proven consistent to experimental and empirical data. Heinze et al. [12] investigated the influence of mesh density and continuous cooling transformation (CCT) behaviour on welding distortion of 5-mm-thick S355J2+N steel numerically and experimentally. Asadi and Goldak [13] proposed a surrogate model to minimize the distortion in a pipe girth weld with 6 sub-passes by analysing only 14 combinations of sub-passes from the total of 48 possible combinations. The pseudo-linear equivalent constant rigidity concept has been used in a thermo-mechanical analysis of plates undergoing welding with simultaneous heat sinking as a method of distortion mitigation [14]. The proposed concept was found to be computationally more efficient and simpler to model compared to FEM for solving similar thermo-elasto-plastic nonlinear problems.

Not only the welding distortion has been studied but the residual stresses have also been investigated by researchers. Residual stresses are stresses that remain in a solid material after the original cause of the stresses has been removed. Heat from welding may cause localized expansion, which is taken up during welding by either the molten metal or the placement of parts being welded. When the finished weldment cools,

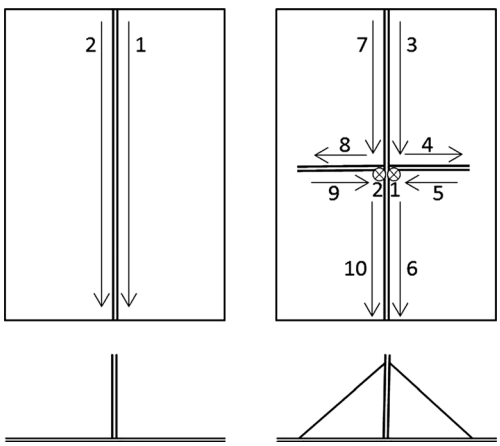

Fig. 1 Specimen models of stiffened plate model 1 (*left*) and model 2 (*right*) and their welding sequences

Table 2 Welding conditions (mean values)

Model	Weld	Current (A)	Voltage	Speed (mm/s)
1	1	220	23	6.33
1	2	160	20	6.76
2	1, 2	190	21	9.00
2	3, 6	220	23	6.05
2	4, 5	220	23	5.83
2	7, 8, 9, 10	210	22	7.10

some areas cool and contract more than others, leaving residual stresses. Systematic studies have shown that the undesirable residual stress may result in failure mechanisms that are sensitive to localized stresses, such as fatigue, brittle fracture, stress corrosion cracking and creep cracking [15].

Liu et al. [16] predicted the residual stress field in the autogenous laser welding process by FEM and verified the results with experimental measurements by an X-ray diffraction technique. The dissimilar metal joints between QCr0.8 copper alloy and 304 SS butt-welded plates were studied numerically and experimentally by electron beam welding with filler wire (EBFW) [17]. The longitudinal residual stress, generally the most harmful to the integrity of the structure among the stress components, was 53 MPa lower in EBFW than that of autogenous electron beam welding (AEBW). In particular, the measurement of residual stress in welded plates requires costly equipment and qualified technicians [18, 19]. Thus, many researchers use simplified mathematic models to represent the residual stress distributed in a plate instead [20–24]. A 2D parametric relationship of residual stress in stiffened plates was developed in [25], based on 12 case studies accounting for various plate thicknesses and welding sequences.

Steel brackets are customarily used to prevent sideways deformation or lateral-torsional buckling in the supporting components of structures such as ships and offshore platforms [26]. The objective of this work is to investigate numerically and experimentally the effect of the presence of the triangular brackets on the weld-induced deformation and residual stress in the stiffened plates.

Fig. 2 Agilent 34970A data acquisition/switch unit

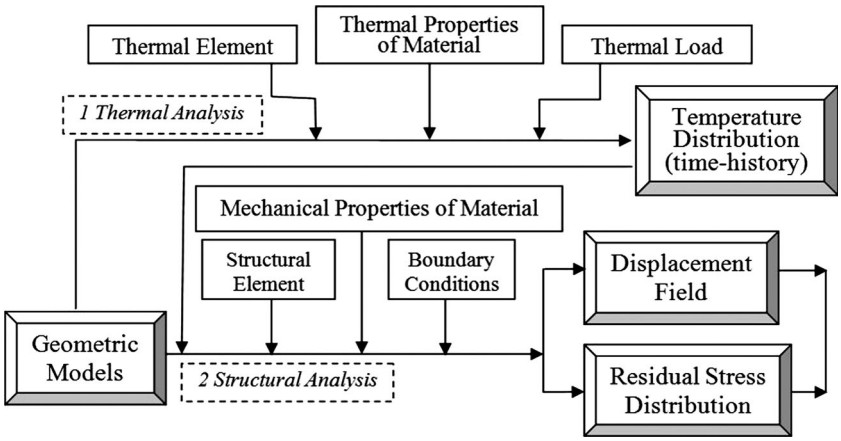

Fig. 3 Flow diagram of transient thermo-elasto-plastic method

2 Experimental setup

The stiffened plates analysed in the present study were fabricated from hot-roll ASTM A36 structural steel. Table 1 lists the configuration of the stiffened plates. The thickness of the plate and stiffener is 9 mm and that of the bracket is 4 mm. In the case of stiffened plate without bracket (entitled as Model 1), one side of the stiffener is welded firstly, and the other side is completed in the same direction after a short interval, as indicated in Fig. 1. In the case of stiffened plate with two brackets located on both sides of the stiffener (entitled as Model 2), the brackets are firstly welded in the vertical directions before starting to weld the stiffener. The conditions of the single-pass gas metal arc welding (GMAW) process are listed in Table 2. In the welding tests, the premixed 80 % Argon and 20 % carbon dioxide is used as the shield gas. The wire is Lincoln S300-RW with 1.0 mm diameter.

K-type Agilent 34307A thermocouple wires were used to measure the temperature histories of the plate specimens during the welding process. The thermocouples were welded to the specimens by Thermocouple Welder. Agilent 34970A data acquisition unit (see Fig. 2) was used to record the temperature data of the selected points. The post-welding deformations were measured by digital dial indicators.

3 Finite element analysis

3.1 Numerical approach

A single directional coupled thermo-elasto-plastic method is adopted to simplify the welding simulation. The thermal and structural analyses are performed separately, as indicated in Fig. 3. It is assumed that the structural result has an effect on the thermal changes. The temperature histories of all nodes are firstly calculated from the thermal analysis and then applied as body loads in the same geometric model to complete the mechanical analysis.

Table 3 Chemical compositions (mass %) of ASTM A36 steel [32]

C	Mn	P	S	Si	Ni	Cr	Mo	Cu	Fe
0.16	0.69	0.033	0.039	0.21	<0.10	<0.08	<0.10	<0.10	Bal.

3.2 Modelling of the heat source

Rosenthal [27] firstly developed an analytical solution for temperature fields. However, the solution is not appropriate near the weld due to its simplification of the heat source geometry and its neglect of the temperature dependency of the thermal properties. The analytical solution is not discussed in the current work.

The 3D double ellipsoidal model [6] is used in the present work to simulate the moving heat source. This model predicts the temperature gradients in front of the arc as steeper than in the rear part, which is identical to

Table 4 Material properties of ASTM A36 steel [32]

T (°C)	C (J/Kg/°C)	K (W/m/°C)	α (10^{-6}/°C)	σy (MPa)	E (GPa)
20	450	51	11.2	380	210
100	475	50	11.8	340	195
210	530	49	12.4	320	195
330	560	46	13.1	262	185
420	630	41	13.6	190	168
540	720	38	14.1	145	118
660	830	34	14.6	75	52
780	910	28	14.6	40	12
985	1055	25	14.6	38	11.8
1320	2000	32	14.6	28	10.4
1420	2100	42	14.6	25	10.2
1500	2150	42	14.6	20	10

T temperature, C specific heat, K thermal conductivity, α expansion coefficient, σy yield stress, E modulus of elasticity

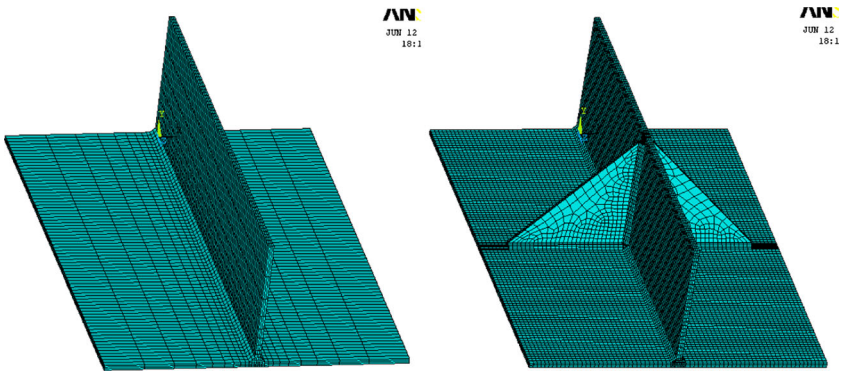

Fig. 4 Finite element model of models 1 and 2

the experimental observations. The heat flux distribution is Gaussian along the longitudinal axis; the front half of the heat source is the quadrant of one ellipsoidal source while the rear half is the quadrant of another ellipsoidal source.

For a point within the first/second semi-ellipsoid located in the front/rear section of the welding arc, the volumetric heat flux equations are described as:

$$q_f(x,y,z) = \frac{6\sqrt{3}\left(f_f Q\right)}{a_f bc\pi^{3/2}} \exp\left(-\frac{3x^2}{b^2} - \frac{3y^2}{a_f^2} - \frac{3z^2}{c^2}\right), y \geq 0 \quad (1)$$

$$q_r(x,y,z) = \frac{6\sqrt{3}(f_r Q)}{a_r bc\pi^{3/2}} \exp\left(-\frac{3x^2}{b^2} - \frac{3y^2}{a_r^2} - \frac{3z^2}{c^2}\right), y < 0 \quad (2)$$

where Q is the power of the heat source; a_f, a_r, b and c are characteristic sizes of the weld pool; f_f and f_r are the heat input proportion in the front/rear part, and $f_f + f_r = 2$. The parameters of the heat source can be adjusted to create a desired molten zone according to the welding conditions. For instance, Goldak et al. [6] concluded that values of $f_f = 0.6$ and $f_r = 1.4$ were found to provide the best correspondence between the measured and calculated thermal history results. In the current calculations, the parameters ($a_f = b = c = 4$ mm and $a_r = 16$ mm) are used.

Using ANSYS Parametric Design Language (APDL) code, the heat source centre (origin of the local coordinate system) changes continuously at every small time increment so that the movement of the heat source can be well simulated. The arc efficiency is estimated as 0.7 for the GMAW process.

3.3 Temperature-dependent material properties

The chemical compositions and material properties of the studied steel plates are listed in Tables 3 and 4. As indicated in Table 4, both thermal and mechanical properties of the material are highly temperature dependent. For instance, the yield stress of the steel is 380 MPa in the room temperature. But it becomes only a half of the original value in a higher 420 °C temperature and even reduces more than 90 % when the temperature increases to 1000 °C and above.

It is noted that the specific heat and the coefficient of thermal expansion increase as the temperature increases, whereas the yield strength, modulus of elasticity and thermal conductivity of the steel have contrary behaviours. To achieve an accurate prediction to responses of a structure subjected to the welding process, the temperature-dependent material properties must be taken into consideration. In the nonlinear stress-strain material models, the work hardening plastic behaviour has to be

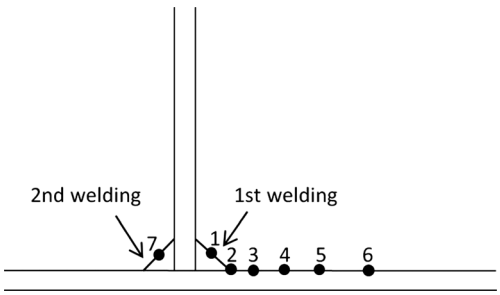

Fig. 5 Selected points for temperature measurements, model 1

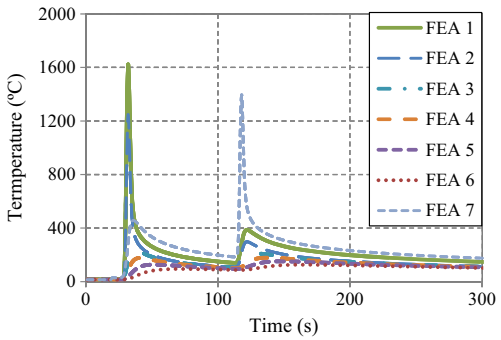

Fig. 6 Temperature curves with respect to time, model 1

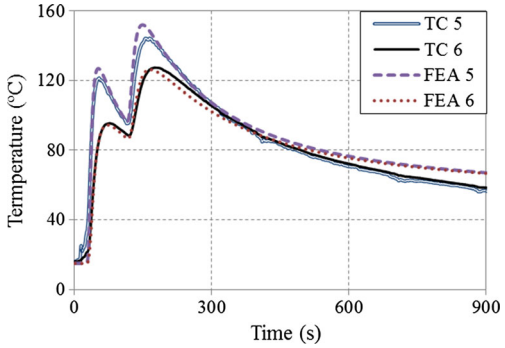

Fig. 7 Comparison between calculated and measured temperatures, model 1

taken into account [28–30]. Bilinear isotropic hardening using von Mises yield criteria is considered in the present numerical calculations.

3.4 Finite element model

Figure 4 shows the finite element (FE) models of the welding specimen model 1 (no brackets) and model 2 (with brackets). A sensitivity analysis of the element size revealed that fine mesh is required in the fusion zone (FZ) and heat-affected zone (HAZ), as well as along the thickness direction. The minimum element size in the current analyses is 1 mm when the specimen has a length of 500 mm. The fillet welds in both models are modelled as small triangles with equal legs. To perform the thermal analysis, 3D brick thermal element Solid 70 was used in ANSYS, before being converted to the corresponding structural element (Solid 185) in the subsequent mechanical analysis. The 3D thermal element Solid 70 has eight nodes with a single degree of freedom, temperature, at each node. The element Solid 185 is an eight-node 3D element with plasticity, hyper-elasticity, stress stiffening, creep, large deflection and large strain capabilities.

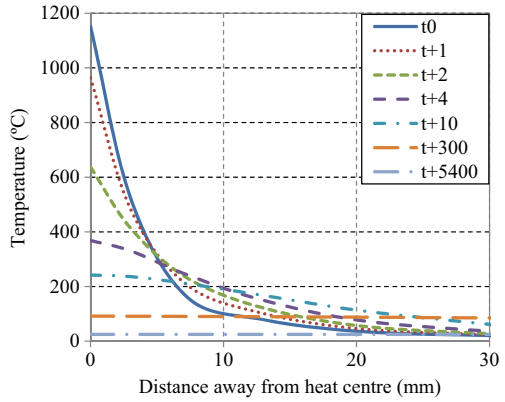

Fig. 8 Temperature distribution in different time steps, model 1

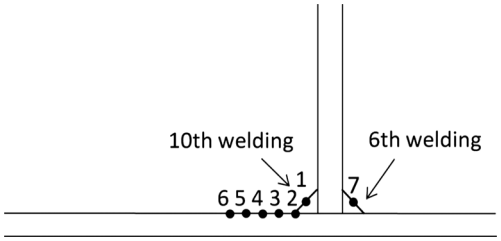

Fig. 9 Selected points for temperature measurements, model 2

4 Thermal results and verification

4.1 Model 1

Figure 5 shows the locations of six selected points in the cross-section of the stiffened plate without brackets for the temperature measurements. Points 1 and 7 locate in the middle of the weld face, point 2 in the lower weld toe, and points 3–6 are 5, 10, 20, and 30 mm away from the lower weld toe, respectively. Due to the molten pool in FZ, only temperatures in points 5 and 6 were measured during the welding experiment.

The temperature time-history curves of the points predicted by FEM are plotted in Fig. 6. Extremely high temperature (over 1600 °C) is observed in the centre of FZ when the welding heat source passes the section in the first welding process, but then a sharp decrease occurs. The effect of heating decreases very rapidly when the distance between the measured point and the weld joint increases. In point 6 (28 mm away from the weld toe), the maximum temperature during the welding process is less than 130 °C. Second peak values are observed at about 120 s in all curves due to the performance of the second welding on the other weld joint. In point 7 where the second welding was performing, the maximum temperature is less than that of the first pass since the heat input is lower compared with the first welding (see Table 2).

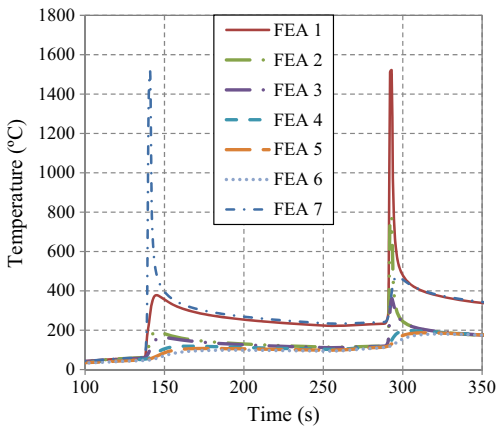

Fig. 10 Temperatures curves with respect to time, Model 2

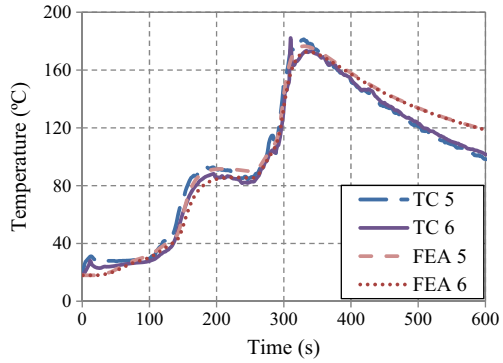

Fig. 11 Comparison between calculated and measured temperatures, model 2

The FEA results have a good agreement with the experimental data (see Fig. 7) despite some differences in the cooling part of the curves due to the heat convection, which indicates a good ability of the current numerical approach to simulate the welding process. Contrary to the temperatures in FZ and HAZ, the second peak values of points 5 and 6 are higher than the first ones, due to the low temperatures outside HAZ in the first welding.

Figure 8 plots the temperature distributions at the top surface of the plate of a reference plane along the transversal direction. The maximum temperature decreased rapidly with time. After 300 s (5 min), a uniform behaviour of the temperature is observed. The welded plate is cooled near the room temperature after an hour and a half.

4.2 Model 2

The locations of the selected points in model 2 are shown in Fig. 9. Points 3–6 are 5, 10, 15 and 20 mm away from the lower weld toe, respectively. Two thermocouple wires are connected in points 5 and 6, in the cross-section in the second half of the plate in terms of the welding direction. Figure 10 plots the temperature time-history predictions of the selected points in the cross-section of the stiffened plate with brackets. The maximum temperature is slightly lower than that of model 1 due to the higher welding speed.

Figure 11 shows the comparison of temperatures between numerical predictions and experimental measurements, in which a good agreement is observed. It is noted that there is no significant difference between the temperatures of points 5 and 6, due to the welding of the brackets in transverse direction.

5 Discussion on residual stress

5.1 Model 1

Figure 12 plots the longitudinal residual stress distributed in the stiffened plate. Significant high tensile stresses are observed in the welds except in the start and end sections. The magnitude of the maximum residual stress (360 MPa) is close to the yield stress of the material (380 MPa). High compressive stresses (max. 133 MPa)

Fig. 12 Longitudinal residual stress distribution, model 1

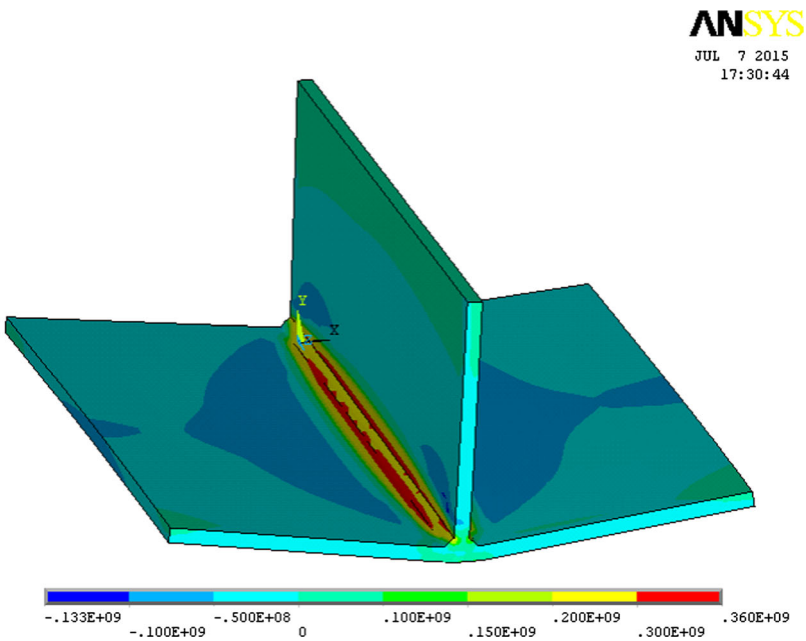

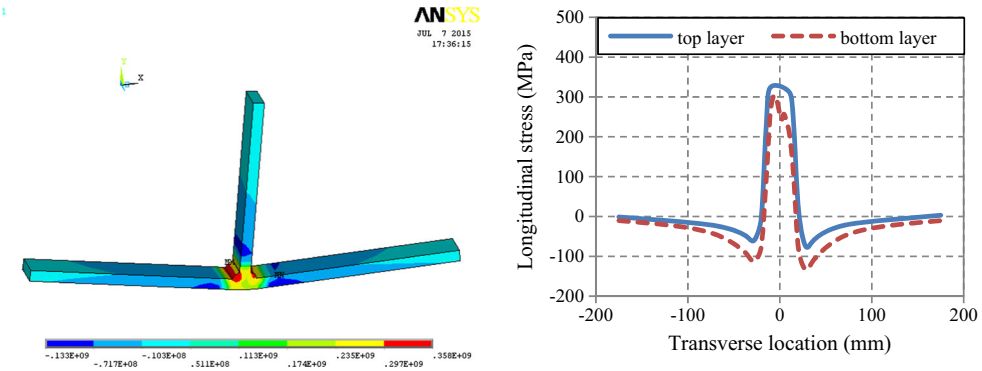

Fig. 13 Longitudinal residual stress distribution at mid-section, model 1

occur in the regions near the welds, while in the transverse edges, the longitudinal stresses become very small.

The residual stress distribution at mid-section of the stiffened plate is shown in Fig. 13. The width of the tension zone is approximately equal to 40 mm. There is an obvious difference between the stresses in the top and bottom layers, especially in terms of the maximum compressive stress.

5.2 Idealized model

In the idealized model suggested by International Ship and Offshore Structures Congress (ISSC) [31], the distribution of welding induced residual stress was idealized as the combination of both tensile and compressive rectangular blocks. The tensile stresses occur in the weld and can be assumed as the yield stress of the material. The magnitude of compressive residual stress is obtained by the equilibrium requirement for the tensile and compressive parts as follows:

$$\sigma_{cp} = \frac{2b_t}{b-2b_t}\sigma_{Yp} \tag{3}$$

where σ_{Yp} is the yield stress of the material, σ_{cp} is the determined compressive stress, b is the width of the associated plate and b_t represents half of the width of the tensile zone.

The parameter b_t plays an essential role on the shape of the residual stress distribution and is suggested as:

$$b_t = \frac{t_w}{2} + \frac{0.26 \times 78.8l^2}{t_w + 2t_p} \tag{4}$$

$$l = \begin{cases} 0.7 \times t_w & \text{when} \quad t_w < 10 \text{ mm} \\ 7.0 & \text{when} \quad t_w \geq 10 \text{ mm} \end{cases} \tag{5}$$

where t_w and t_p are the thicknesses of the plate and stiffener, respectively.

Figure 14 plots the residual stress distribution suggested by ISSC [31], comparing with the numerical results. However, it is observed that the ISSC curve overestimate the maximum tensile stress and the width of the tensile zone (71.2 mm). In addition, the engineering curve neglects the transformations of the compressive residual stress along the width of the associated plate.

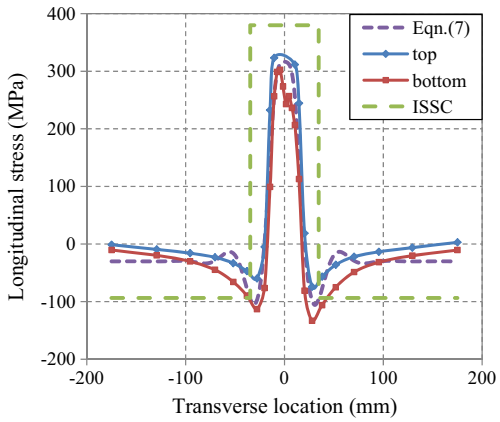

Fig. 14 Comparison of longitudinal residual stress at mid-section, model 1

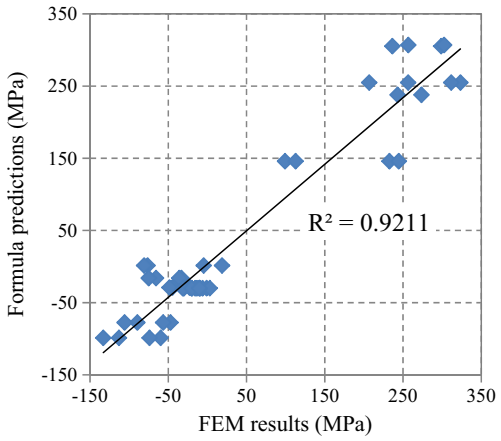

Fig. 15 Comparison of residual stresses, model 1

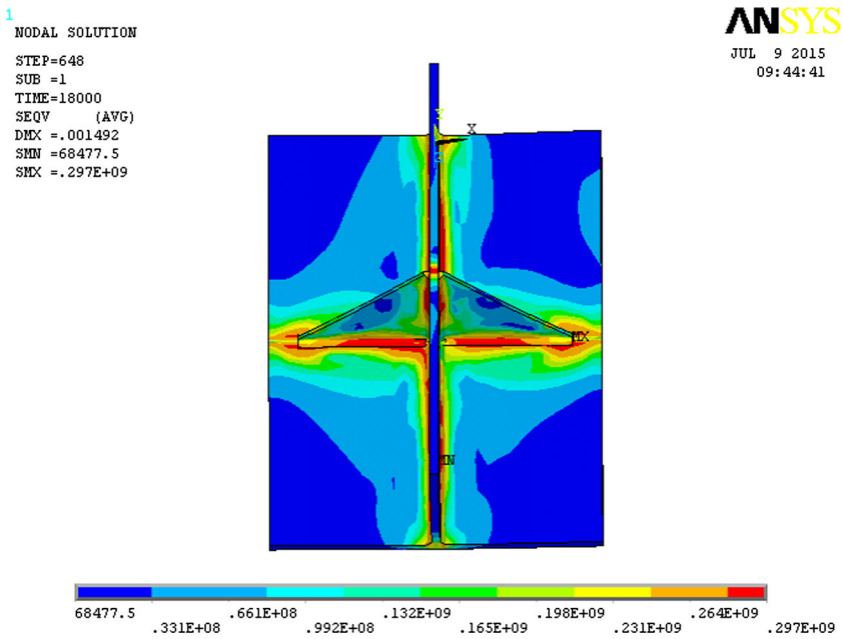

Fig. 16 von Mises residual stress distribution, model 2

To have a better description of the residual stress distribution, a new formula was proposed based on the formula proposed in [25] considering five parameters representing different details in the true curve.

$$\sigma_r(x,y) = k\sigma_y \exp\left(-\frac{|x|}{\tau}\right)\cos\left(\frac{\pi|x|}{m}-\alpha\right)-\beta \tag{6}$$

where k is a scale factor, σ_y is the yield stress of the material, x is the longitudinal coordinate, τ stands for a half of the width in the tensile region, m is a factor for the transverse transformations and α and β are controlling parameters defined from the regression analysis.

By fitting to the present FEM result, Eq. (6) becomes

$$\sigma_r(x,y) = 1.7\sigma_y \exp\left(-\frac{|x|}{16}\right)\cos\left(\frac{\pi|x|}{25}-1.2\right)-30 \tag{7}$$

The new longitudinal residual stress at mid-section is also plotted in Fig. 14. It is observed that all significant

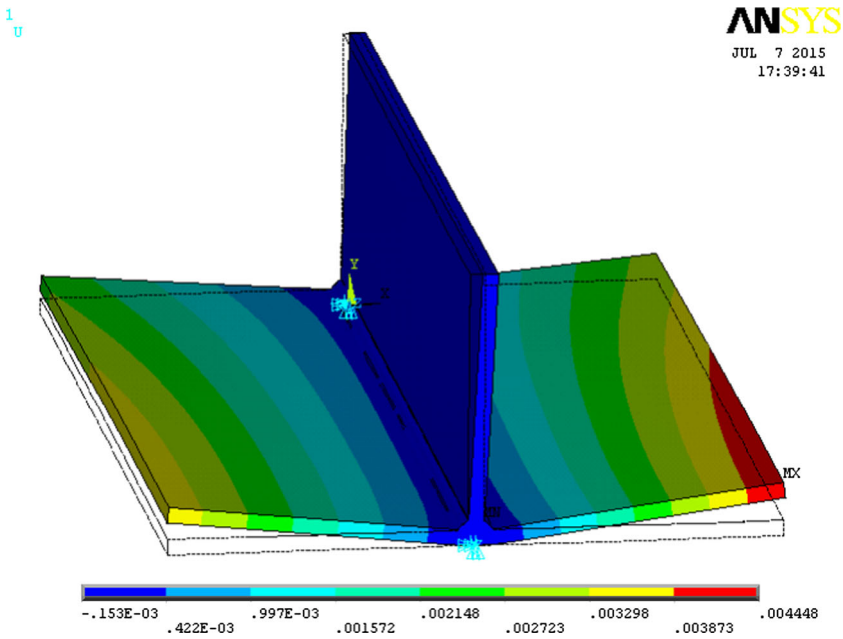

Fig. 17 Vertical deformation, model 1

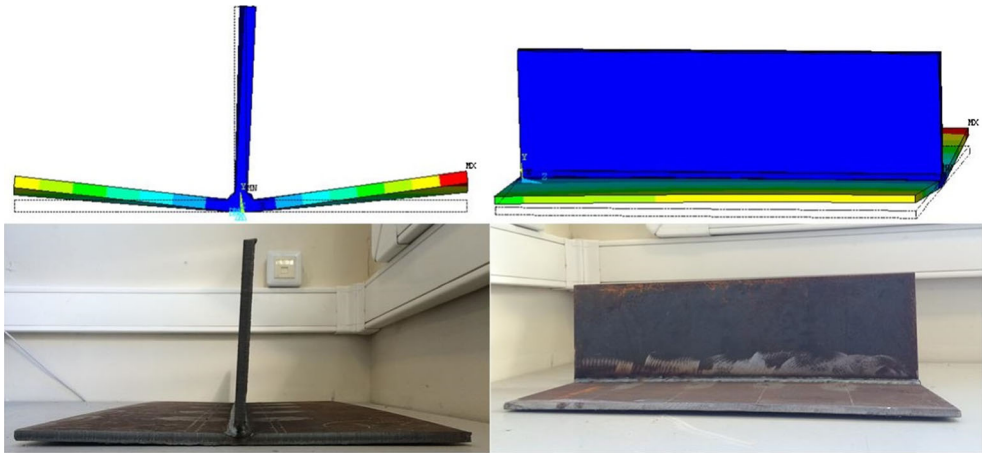

Fig. 18 Stiffened plate after welding, model 1

characteristics of the residual stress distribution are successfully predicted, including the maximum tensile and compressive stress, and the sharply transformation from tension to compression zone. The predicted width of the tensile zone (32 mm) is much more accurate than the ISSC curves. Comparing the predicted residual stresses by this regression equation with the numerical results, the coefficient of determination *R*-square factor is 0.921 (see Fig. 15), which indicates a very good agreement between the two sets of data.

5.3 Model 2

Figure 16 plots the distribution of the von Mises stress in the stiffened plate with brackets (model 2). Significantly high stresses appear in the welding lines due to the contraction after the cooling stage. The stress reduces gradually in the HAF but then drops rapids in other region of the structure until reaching the minimum value in the four corners. The maximum value of the von Mises stress is 297 MPa and is in the same level as that of model 1 (298 MPa).

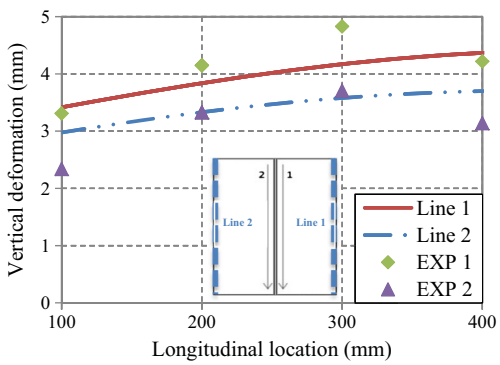

Fig. 19 Comparison between predicted and measured vertical deformation, model 1

6 Weld-induced deformations

6.1 Model 1

In general, the vertical deformation of model 1 has a quasi-linear behaviour from the weld centre to the transverse edges (see Fig. 17 with scale factor 5). Two points in the start/end section of the plate were fixed during the calculation to prevent the rigid body motion. There is almost no deformation in the middle of the cross-sections due to the constraints, while maximum vertical deformations occur in the transverse edges of the associated plate.

Figure 18 plots the deformed shapes of the welded plate (with scale factor 5 in the finite element models). The weld joint is twisted since the angular distortions in both sides do not occur simultaneously. A relatively good agreement is observed between the numerical results and the experimental measurements, as indicated in Fig. 19. Along the longitudinal direction in the edges, slight bigger deformations occur in the middle. It is explained as the difference between the boundary condition used in the FE model and the real condition in the workshop. The FE model has limited longitudinal shrinkage due to the constrained points and thus relatively smaller degree of curvature in vertical deformation.

6.2 Model 2

Figure 20 plots the deformed shapes of the welded plate with brackets. Small deformations appear in the four corners of the associated plate, among which the maximum vertical deformation is 1.49 mm. Along the longitudinal direction of the edges, smaller vertical deformations occur in the middle due to the existence of the brackets.

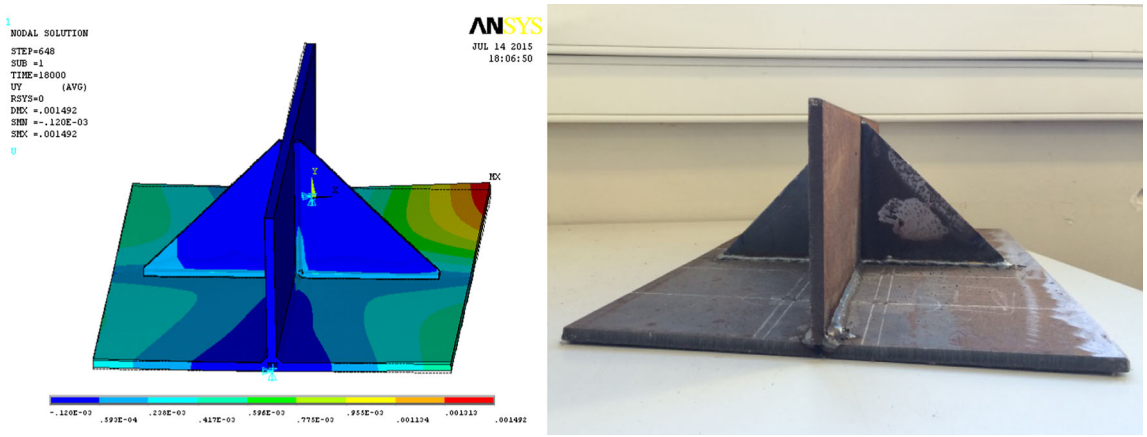

Fig. 20 Stiffened plate after welding, model 2

The comparison between the numerical results and the experimental measurements in model 2 is shown in Fig. 21. Compared with the results of model 1, it is observed that with two transverse brackets, the maximum vertical deformation reduces 74 % in the experimental measurements and 67 % in the numerical simulation.

7 Conclusions

3D thermo-elasto-plastic finite element analyses have been performed to predict the distribution of the welding deformation and residual stress and distortion in two stiffened plates (one of them with transverse brackets). Experimental welding tests are designed to evaluate the effect of the presence of the triangular brackets on the weld-induced deformation and residual stress in the stiffened plates.

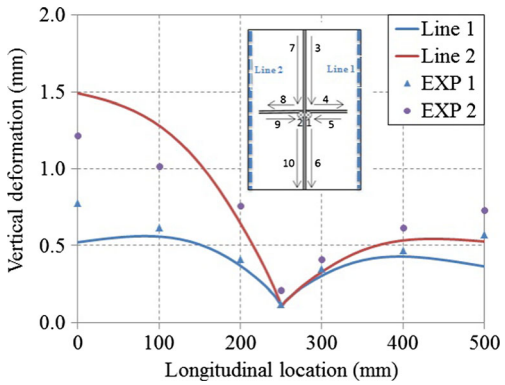

Fig. 21 Comparison between predicted and measured vertical deformation, model 2

Good agreement are observed between the present numerical results and experimental measurements with respect to the temperature distributions and weld-induced vertical deformation leading to the conclusion that the finite element model developed in the current study can be effectively used to predict the behaviour of out-of-plane deformation in the fillet welded structures.

An empirical formula is proposed in the present work and is proved to have the ability to provide accurate prediction of the residual stress distributed in the stiffened plate.

The presence of the brackets has small influence on the residual stress distribution in the stiffened plate. However, with two transverse brackets, the maximum deformation reduces 74 % in the experimental measurements and 67 % in the numerical simulation.

Acknowledgments The first author has been funded by a PhD scholarship from ABS, the American Bureau of Shipping.

References

1. Chen BQ, Hashemzadeh M, Guedes Soares C (2014) Numerical analysis of the effects of weld parameters on distortions and residual stresses in butt welded steel plates. In: Guedes Soares C, Lopes Pena F (eds) Developments in maritime transportation and exploitation of sea resources. Taylor & Francis Group, London, pp 309–320
2. Gannon L, Liu Y, Pegg N, Smith MJ (2010) Effect of welding sequence on residual stress and distortion in flat-bar stiffened plates. Mar Struct 23:385–404
3. Kmiecik M, Jastrzebski T, Kuzniar J (1995) Statistics of ship plating distortions. Mar Struct 58:119–132

4. Chen BQ, Garbatov Y, Guedes Soares C (2011) Measurement of weld induced deformations in three-dimensional structures based on photogrammetry technique. J Ship Prod Des 27:51–62
5. Chen BQ, Guedes Soares C (2014) Deformation measurements in welded plates based on close-range photogrammetry. Proceedings of the Institution of Mechanical Engineers, Part B: Journal of Engineering Manufacture. doi: 10.1177/0954405414558734
6. Goldak JA, Chakravarti A, Bibby MJ (1984) A new finite element model for welding heat source. Metall Trans B 15B:299–305
7. Chen BQ, Hashemzadeh M, Guedes Soares C (2014) Numerical and experimental studies on temperature and distortion patterns in butt-welded plates. Int J Adv Manuf Technol 72:1121–1131
8. Hashemzadeh M, Chen BQ, Guedes Soares C (2014) Comparison between different heat source types in thin-plate welding simulation. In: Guedes Soares C, Lopez Pena F (eds) Developments in maritime transportation and exploitation of Sea resources. Taylor & Francis Group, London, pp 329–336
9. Hashemzadeh M, Chen BQ, Guedes Soares C (2015) Numerical and experimental study on butt weld with dissimilar thickness of thin stainless steel plate. Int J Adv Manuf Technol 78:319–330
10. Ueda Y, Yamakawa T (1971) Analysis of thermal elastic-plastic stress and strain during welding by finite element method. Trans Jpn Weld Soc 2(2):186–196
11. Michaleris P, DeBiccari A (1997) Prediction of welding distortion. Weld Res Suppl 76:172–181
12. Heinze C, Schwenk C, Rethmeier M (2011) Influences of mesh density and transformation behavior on the result quality of numerical calculation of welding induced distortion. Simul Model Pract Theory 19:1847–1859
13. Asadi M, Goldak JA (2011) Combinatorial optimization of weld sequence by using a surrogate model to mitigate a weld distortion. Int J Mech Mater Des 7:123–139
14. Adak M, Mandal NR (2010) Numerical and experimental study of mitigation of welding distortion. Appl Math Model 34:146–158
15. Estefen SF, Gurova T, Werneck D, Leontiev A (2012) Welding stress relaxation effect in butt-jointed steel plates. Mar Struct 29: 211–225
16. Liu W, Ma J, Kong F, Liu S, Kovacevic R (2015) Numerical modeling and experimental verification of residual stress in autogenous laser welding of high-strength steel. Lasers Manuf Mater Process 2:24–42
17. Zhang BG, Zhao J, Li XP, Chen GQ (2015) Effects of filler wire on residual stress in electron beam welded QCr0.8 copper alloy to 304 stainless steel joints. Appl Therm Eng 80:261–268
18. Kenno SY, Das S, Kennedy JB, Rogge RB, Gharghouri M (2010) Residual stress distributions in ship hull specimens. Mar Struct 23: 263–273
19. Park JU, An G, Woo WC, Choi JH, Ma N (2014) Residual stress measurement in an extra thick multi-pass weld using initial stress integrated inherent strain method. Mar Struct 39:424–437
20. Gannon L, Liu Y, Pegg N, Smith MJ (2012) Effect of welding-induced residual stress and distortion on ship hull girder ultimate strength. Mar Struct 28:25–49
21. Cui W, Mansour AE (1998) Effects of welding distortions and residual stresses on the ultimate strength of long rectangular plates under uniaxial compression. Mar Struct 11:251–269
22. Guedes Soares C, Gordo JM (1997) Design methods for stiffened plates under predominantly uniaxial compression. Mar Struct 10: 465–497
23. Gordo JM, Guedes Soares C, Faulkner D (1996) Approximate assessment of the ultimate longitudinal strength of the hull girder. J Ship Res 40(1):60–69
24. Gordo JM, Guedes Soares C (2009) Tests on ultimate strength hull box girders made of high tensile steel. Mar Struct 22:770–790
25. Chen BQ, Hashemzadeh M, Garbatov Y, Guedes Soares C (2014) Numerical and parametric modeling and analysis of weld-induced residual stresses. Int J Mech Mater Des. doi: 10.1007/s10999-014-9269-7
26. Lee SE, Thayamballi AK, Paik JK (2015) Ultimate strength of steel brackets in ship structures. Ocean Eng 101:182–200
27. Rosenthal D (1941) Mathematical theory of heat distribution during welding and cutting. Weld J 20(5):220–234
28. Jiang WC, Wang BY, Gong JM, Tu ST (2011) Finite element analysis of the effect of welding heat input and layer number on residual stress in repair welds for a stainless steel clad plate. Mater Des 32: 2851–2857
29. Jiang WC, Luo Y, Wang BY, Woo W, Tu ST (2015) Neutron diffraction measurement and numerical simulation to study the effect of repair depth on residual stress in 316L stainless steel repair weld. J Pressure Vessel Technol 137: 041406-041406-12
30. Sonne MR, Tutuma CC, Hattel JH, Simar A, de Meester B (2013) The effect of hardening laws and thermal softening on modeling residual stresses in FSW of aluminum alloy 2024-T3. J Mater Process Technol 213:477–486
31. Yao T, Astrup OC, Caridis P, et al. (2000) Ultimate hull girder strength. ISSC Special Task Committee VI.2, Proceedings of the 14th International Ship and Offshore Structures Congress, Nagasaki, Japan
32. Chang PH, Teng TL (2004) Numerical and experimental investigations on the residual stresses of the butt-welded joints. Comput Mater Sci 29:511–522